

## ULTRAVIOLET LIGHT FROM YOUNG STARS IN GEMS QUASAR HOST GALAXIES AT $1.8 < z < 2.75$

K. JAHNKE,<sup>1</sup> S. F. SÁNCHEZ,<sup>1</sup> L. WISOTZKI,<sup>1,2</sup> M. BARDEN,<sup>3</sup> S. V. W. BECKWITH,<sup>4,5</sup> E. F. BELL,<sup>3</sup> A. BORCH,<sup>3</sup>  
J. A. R. CALDWELL,<sup>4</sup> B. HÄUSSLER,<sup>3</sup> C. HEYMANS,<sup>3</sup> S. JOGEE,<sup>4</sup> D. H. MCINTOSH,<sup>6</sup> K. MEISENHEIMER,<sup>3</sup>  
C. Y. PENG,<sup>7</sup> H.-W. RIX,<sup>3</sup> R. S. SOMERVILLE,<sup>4</sup> AND C. WOLF<sup>8</sup>

Received 2004 March 18; accepted 2004 June 2

### ABSTRACT

We have performed *Hubble Space Telescope* imaging of a sample of 23 high-redshift ( $1.8 < z < 2.75$ ) active galactic nuclei (AGNs), drawn from the COMBO-17 survey. The sample contains moderately luminous quasars ( $M_B \sim -23$ ). The data are part of the Galaxy Evolution from Morphologies and SEDs imaging survey that provides high-resolution optical images obtained with the Advanced Camera for Surveys in two bands (F606W and F850LP), sampling the rest-frame UV flux of the targets. To deblend the AGN images into nuclear and resolved (host galaxy) components, we use a point-spread function subtraction technique that is strictly conservative with respect to the flux of the host galaxy. We resolve the host galaxies in both filter bands in nine of the 23 AGNs, whereas the remaining 14 objects are considered nondetections, with upper limits of less than 5% of the nuclear flux. However, when we co-add the unresolved AGN images into a single high signal-to-noise ratio composite image, we find again an unambiguously resolved host galaxy. The recovered host galaxies have apparent magnitudes of  $23.0 < F606W < 26.0$  and  $22.5 < F850LP < 24.5$ , with rest-frame UV colors in the range  $-0.2 < (F606W - F850LP)_{\text{obs}} < 2.3$ . The rest-frame absolute magnitudes at 200 nm are  $-20.0 < M_{200 \text{ nm}} < -22.2$ . The photometric properties of the composite host are consistent with the individual resolved host galaxies. We find that the UV colors of all host galaxies are substantially bluer than expected from an old population of stars with formation redshift  $z \leq 5$ , independent of the assumed metallicities. These UV colors and luminosities range up to the values found for Lyman break galaxies (LBGs) at  $z = 3$ . Our results suggest either a recent starburst of, e.g., a few percent of the total stellar mass at 100 Myr before observation, with mass fraction and age strongly degenerate, or the possibility that the detected UV emission may be due to young stars forming continuously. For the latter case we estimate star formation rates of typically  $\sim 6 M_{\odot} \text{ yr}^{-1}$  (uncorrected for internal dust attenuation), which again lies in the range of rates implied from the UV flux of LBGs. Our results agree with the recent discovery of enhanced blue stellar light in AGN hosts at lower redshifts.

*Subject headings:* galaxies: active — galaxies: fundamental parameters — galaxies: high-redshift — galaxies: starburst — quasars: general

*Online material:* color figures

### 1. INTRODUCTION

Around redshifts of  $z \sim 2-3$ , luminous quasars were orders of magnitude more numerous than they are today. Although the physics of how active galactic nuclei (AGNs) evolve is still not understood, several links between galaxy and quasar evolution have emerged over recent years. The observational confirmation of supermassive black holes in the nuclei of all galaxies with a substantial bulge component (e.g., Gebhardt et al. 2000) makes every such galaxy a potential AGN host. The strong evolution of the AGN space density could there-

fore be related to the availability of accretion fuel in the host galaxies or to the frequency of AGN triggering events.

Gravitational interaction and major or minor merging of galaxies have long been suggested as important factors in driving nuclear activity in galaxies. Confirming any of these as the dominant process has proved difficult, mainly because the morphological characteristics found for relatively nearby AGN host galaxies are so diverse. Furthermore, the properties of the hosts in the “heyday” of quasars ( $z \gtrsim 2$ ) are still elusive, a consequence of the substantial observational difficulties. The contrast between the bright nuclear point source and the surrounding galaxy increases dramatically beyond  $z \sim 1$  as a result of both surface brightness dimming and waveband shifts toward the rest-frame UV.

The last years have seen numerous attempts to resolve the host galaxies of high-redshift quasars. Owing to the observational challenges of detecting distant host galaxies, the observational effort for each object is large, and the observed samples have consequently been very small, of the order of  $\lesssim 5$  per target group. While radio-loud quasars appear to be very extended and have been resolved out to  $z \sim 4$  (e.g., Lehnert et al. 1992; Carballo et al. 1998; Hutchings et al. 1999; Kukula et al. 2001; Hutchings 2003; Sánchez & González-Serrano 2003), this is not the case for the large majority of radio-quiet quasars.

<sup>1</sup> Astrophysikalisches Institut Potsdam, An der Sternwarte 16, 14482 Potsdam, Germany; kjahnke@aip.de.

<sup>2</sup> Universität Potsdam, Am Neuen Palais 10, 14469 Potsdam, Germany.

<sup>3</sup> Max-Planck-Institut für Astronomie, Königstuhl 17, 69117 Heidelberg, Germany.

<sup>4</sup> Space Telescope Science Institute, 3700 San Martin Drive, Baltimore, MD 21218.

<sup>5</sup> Johns Hopkins University, 3700 San Martin Drive, Baltimore, MD 21218.

<sup>6</sup> Department of Astronomy, University of Massachusetts, 710 North Pleasant Street, Amherst, MA 01003.

<sup>7</sup> Steward Observatory, University of Arizona, 933 North Cherry Avenue, Tucson, AZ 85721.

<sup>8</sup> Department of Physics, Denys Wilkinson Building, University of Oxford, Keble Road, Oxford OX1 3RH, UK.

At high redshifts two constraints dominate observational studies of host galaxies: On one hand, very good seeing conditions are required to maximize the spatial contrast of the compact nuclear source with the extended host galaxy. On the other, large telescope apertures are preferential for tracing faint quasar hosts to as far away from the nucleus as possible. Thus, significant progress had to wait for 8 m class telescopes at very good sites with active optics systems—with a very high light collecting power but atmospheric seeing limitations—and for the *Hubble Space Telescope* (*HST*) and its high space-based sensitivity combined with unprecedented spatial resolution but limited size, which might miss light from the faint outer structures of the hosts. Some host galaxies of radio-quiet quasars at  $z \simeq 2$  have now been resolved both in the near-infrared (Aretxaga et al. 1998; Kukulka et al. 2001; Ridgway et al. 2001; Falomo et al. 2004) and in the optical domains (Hutchings et al. 2002), showing these objects to be moderately luminous, corresponding to present-day  $L^*$  or slightly brighter.

However, host galaxy colors have been unavailable, precluding estimates of the mass-to-light ratio ( $M/L$ ). Thus, without colors the observed luminosities and their evolution with redshift cannot be mapped to the mass evolution if young stars contribute a major fraction of the AGN host's light. This is important, as several high-luminosity quasars at  $z \gtrsim 2$  appear to be located in very UV-luminous host galaxies (Lehnert et al. 1992; Aretxaga et al. 1998; Hutchings et al. 2002). In addition, at low redshifts there is a link between nuclear activity and enhanced global star formation in the host galaxies. Kauffmann et al. (2003) reported that Sloan Digital Sky Survey spectra of local Seyfert 2 galaxies show a significant contribution from young stellar populations and that this trend is strongly correlated with nuclear luminosity. In a multicolor study of low- $z$  QSO hosts (Jahnke et al. 2004), as well as at intermediate redshifts (Sánchez et al. 2004; see below), we found that hosts of elliptical morphology can be significantly bluer than the bulk of inactive elliptical galaxies. These results indicate that in the recent past the star formation activity in galaxies hosting an AGN may have been different from that of normal galaxies. The details are far from understood. Clearly, more information is required to investigate the relation of star formation and AGN activity, their common cause or causal order, and the evolution of these properties with redshift.

The new generation of wide-field imaging mosaics obtained with the *HST*, especially in conjunction with deep AGN surveys, has opened a new observational avenue toward AGN host galaxy studies. Here we present first results on AGNs within the Galaxy Evolution from Morphologies and SEDs (GEMS) project (Rix et al. 2004), the largest *HST* color mosaic to date. In the present paper we investigate the presence of rest-frame UV light in a substantial sample of  $z > 1.8$  AGNs, all with nuclear luminosities near  $M_B = -23$ . In a companion paper (Sánchez et al. 2004), we study the rest-frame colors and morphological properties of a sample of intermediate-redshift ( $z \lesssim 1$ ) AGNs.

The paper is organized as follows. We first describe the sample selection and properties together with a summary of the observational data (§ 2). We then comment on the decomposition of the nuclear and galaxy contribution, including a brief summary of the extensive simulations that we use to estimate measurement errors (§ 3). In § 4 we present the measured host galaxy magnitudes and describe our treatment of nondetections. We move on to discuss the results in § 5, followed by our conclusions in § 6. We use  $H_0 = 70 \text{ km s}^{-1} \text{ Mpc}^{-1}$ ,  $\Omega_m = 0.3$ , and  $\Omega_\Lambda = 0.7$  throughout this paper. All

quoted magnitudes are zero-pointed to the AB system with  $ZP_{F606W} = 26.493$  and  $ZP_{F850LP} = 24.843$ .

## 2. AGNs IN THE GEMS SURVEY

### 2.1. Overall Survey Properties

GEMS (Rix et al. 2004) is a large imaging survey in two bands (F606W and F850LP) with the Advanced Camera for Surveys (ACS) aboard *HST*. Centered on the Chandra Deep Field–South, it covers an area of  $\sim 28' \times 28'$  (78 ACS fields). Each ACS field was integrated for  $3 \times (12\text{--}13)$  minute exposures per filter (one orbit, dithered by  $3''$  between exposures). The individual images were then combined, corrected for the ACS geometric distortion, and at the same time rebinned to a finer pixel grid of  $0''.03$ , achieving approximate Nyquist sampling of the point-spread function (PSF). The image combination also removed artifacts such as cosmic-ray hits and satellite trails. The resulting point-source limiting magnitudes are  $m_{AB}(F606W) = 28.3$  ( $5 \sigma$ ) and  $m_{AB}(F850LP) = 27.1$  ( $5 \sigma$ ). In its central  $\sim \frac{1}{5}$ , GEMS incorporates the epoch 1 data from the GOODS (Giavalisco et al. 2004) project, which are similarly deep as the other GEMS fields. Further details of the data reduction procedure will be given in a forthcoming paper (J. A. R. Caldwell et al. 2004, in preparation).

The area covered by GEMS coincides with one of four fields covered by the COMBO-17 survey (Wolf et al. 2004), which produced a low-resolution spectrophotometric database (based on photometry in 17 filters) for about 10,000 galaxies and 60 type 1 AGNs brighter than  $R \leq 24$  (Vega zero point) in the Chandra Deep Field–South area (Wolf et al. 2003b, 2004). The large number of filters permitted simultaneous assignment of accurate spectral energy distributions (SEDs) and redshifts for both galaxies and type 1 AGNs. Galaxies and AGNs are classified by matching an SED template library to the set of 17 photometric points. The AGN SED is composed of a range of continuum spectra with added broad emission lines (all details are given in Wolf et al. 2004). Type 2 AGNs, as well as very low luminosity AGNs, are invariably classified as galaxies. COMBO-17 photometric redshifts are very reliable, with an rms scatter of  $\sigma_z/(1+z) \simeq 0.02$  for galaxies (at  $z < 1.2$ ) and  $\sigma_z/(1+z) \simeq 0.03$  for AGNs at all redshifts. In this paper we address specific COMBO-17 sources just by their running identifiers; the full COMBO-17 list of classifications in the Chandra Deep Field–South is available in Wolf et al. (2004).

### 2.2. The AGN Sample

The COMBO-17–selected AGNs in the GEMS field range over redshifts from  $z \simeq 0.5$  up to  $z \simeq 4$ . In this study we investigate the high- $z$  part of the AGN distribution. Our sample contains all AGNs brighter than  $R = 24$  in the redshift range  $1.8 < z < 2.75$  that show a meaningful counterpart in the GEMS images. This excludes three objects with primary classifications as AGNs by COMBO-17 that were apparently low-redshift ( $z \sim 0.1$ ) emission-line galaxies.

At these redshifts, all light detected in the GEMS bands will originate in the rest-frame UV. In fact, the lower redshift limit has been imposed to ensure that the long-wavelength cutoff of the F850LP filter is still located below the Balmer jump for all objects. The upper redshift boundary, on the other hand, was set to avoid contamination from possible extended Ly $\alpha$  emission in the F606W filter. The resulting sample contains 23 AGNs, three of which are positioned in the overlap region of two tiles so that two separate images exist for these. One object

TABLE 1  
OBJECTS OF THE SAMPLE

ID <sup>a</sup>	Tile <sup>b</sup>	R.A. (J2000.0)	Decl. (J2000.0)	$z^c$	$R$ (Vega) <sup>d</sup>	F606W <sup>e</sup>	F850LP <sup>e</sup>
12325.....	11	03 33 01.7	-27 58 19	1.843	20.38	20.13	19.65
19965.....	23	03 31 45.2	-27 54 36	1.90	19.96	20.59	20.29
30792.....	82	03 32 43.3	-27 49 14	1.929	22.36	21.60	22.06
02006.....	04	03 32 32.0	-28 03 10	1.966	19.76	19.59	18.98
04809.....	08	03 31 36.3	-28 01 50	1.988	22.31	21.18	20.91
06817.....	09	03 31 27.8	-28 00 51	1.988	21.59	21.61	20.86
18324.....	19	03 33 00.9	-27 55 22	1.990	22.58	22.00	21.33
05498.....	01	03 33 16.1	-28 01 31	2.075	22.29	22.91	22.28
11941.....	10	03 33 26.3	-27 58 30	2.172	20.51	20.80	20.40
62127.....	62	03 31 36.7	-27 34 46	2.175	23.57	24.91	24.37
51835.....	55	03 31 40.1	-27 39 17	2.179	22.92	23.01	22.41
00784.....	05	03 32 27.1	-28 03 36	2.282	23.29	23.28	22.80
36120.....	39	03 31 49.4	-27 46 34	2.306	22.37	22.70	22.23
05696.....	02	03 33 21.8	-28 01 21	2.386	23.06	22.73	22.32
05696.....	03	03 33 21.8	-28 01 21	2.386	23.06	23.14	22.68
07671.....	07	03 31 51.8	-28 00 26	2.436	22.35	22.35	22.24
07671.....	15	03 31 51.8	-28 00 26	2.436	22.35	22.36	22.22
06735.....	02	03 33 06.3	-28 00 56	2.444	21.98	22.14	21.88
01387.....	08	03 31 44.0	-28 03 20	2.503	23.24	24.05	23.17
33644.....	31	03 32 59.9	-27 47 48	2.538	21.87	21.28	21.17
11922.....	11	03 33 09.1	-27 58 27	2.539	22.25	22.65	21.93
16621.....	19	03 33 09.7	-27 56 14	2.540	19.98	20.41	20.06
15396.....	21	03 32 16.2	-27 56 44	2.682	22.64	22.69	22.41
33630.....	33	03 31 40.1	-27 47 46	2.719	21.74	22.21	21.98
42882.....	45	03 32 01.6	-27 43 28	2.719	23.18	23.89	23.48
42882.....	95	03 32 01.6	-27 43 28	2.719	23.18	24.04	23.54

NOTE.—Units of right ascension are hours, minutes, and seconds, and units of declination are degrees, arcminutes, and arcseconds.

<sup>a</sup> ID from the COMBO-17 catalog.

<sup>b</sup> GEMS tile number (1–63 GEMS, 80–95 GOODS region).

<sup>c</sup> Photometric redshift from COMBO-17; for COMBO-17 19965, a revised redshift from an ongoing objective prism survey was used.

<sup>d</sup>  $R$ -band magnitude (Vega zero point) from COMBO-17.

<sup>e</sup> Total F606W- and F850LP-band magnitudes (AB zero point) as measured with the ACS. Photometric errors range from 0.07 to 0.10 for both filters. Three objects are imaged on two different tiles. Because of nuclear variability, this can result in different F606W- and F850LP-band fluxes.

(COMBO-17 05696) shows inconsistent photometry between the two tiles due to variability over the 111 days between the two integrations. Another object (COMBO-17 19965) was classified in COMBO-17 with a redshift of  $z = 0.634$  that had to be revised following spectroscopy observations (G. Worseck 2004, private communication) and is now entered in this sample with  $z = 1.90$ . Table 1 gives an overview of the sample properties, and Figure 1 shows the distribution in  $R$  and  $z$ . The average absolute magnitudes for these objects, which we call intermediately luminous quasars, place them close to the canonical division of  $M_B \simeq -23$  between Seyfert galaxies (low luminosity) and QSOs (high luminosity).

Several X-ray sources in the Chandra Deep Field–South have already been studied by *HST* with the WFPC2 (Schreier et al. 2001; Koekemoer et al. 2002; Grogin et al. 2003), most of them faint AGNs, but their sample is completely disjoint from the COMBO-17 AGN selection for this redshift range. One object falls into our redshift range but has  $R > 24$ , outside our selection limits.

### 3. DATA ANALYSIS

#### 3.1. Background and Variances

Even though space-based, ACS shows a nonnegligible background from stray light. In the initial reduction process, a global, outlier-clipped median background is subtracted (J. A. R.

Caldwell et al. 2004, in preparation). As the deblending of nuclear and host galaxy components with two-dimensional modeling is sensitive to background sources, we applied an extra procedure to remove net residuals in the local background. This included an iterative masking of all objects in the field and the determination of the local background from the object-free regions. For each square of  $200 \times 200$  pixels, an average from the unmasked pixels was computed, with a subsequent bilinear interpolation between these values to yield a background estimate for the whole field. After background adjustment, small subimages of  $128 \times 128$  pixels were extracted around all AGNs, corresponding to a field of view of  $3''.84 \times 3''.84$ . This field size contains  $\geq 99\%$  of the ACS PSF flux. Since the AGNs are not strongly resolved, this fraction also applies to the AGN flux.

The data reduction procedure kept record of the individual pixel weights throughout the process of reduction and combination. This information was then used in combination with the shot noise derived from pixel count rates to construct variance images that were later used in the error budget calculations.

#### 3.2. PSF Estimation

Compared to ground-based telescopes, the PSF of ACS is very stable in time. However, coma, astigmatism, and defocus from surface height variations of the two CCDs lead to

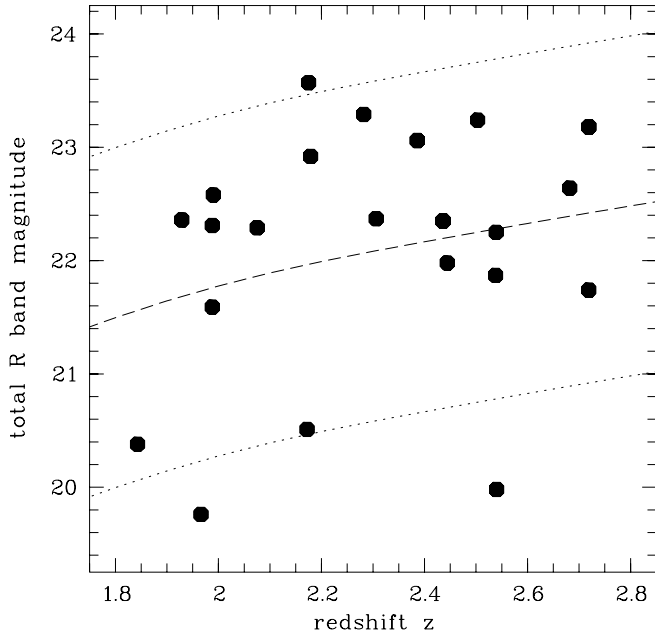


FIG. 1.—COMBO-17 redshifts and  $R$  magnitudes of the AGNs in the sample. The dashed line marks the expected  $R$ -band magnitude for an AGN of  $M_B = -23$  at the corresponding redshifts, assuming a typical quasar spectrum (Wolf et al. 2003a), and the dotted lines correspond to  $M_B = -21.5$  and  $-24.5$  for reference.

variations over the field of view that need to be taken into account. The variations are much weaker than for the WFPC2 but remain nonnegligible. In addition, the “breathing” of *HST* changes the focal length, which leads also to a small time variability in the PSF. In Figure 2 we show the mean ACS PSF compiled from  $\sim 500$  stars in the extensive GEMS area and the variation of the PSF over the field of view.

The variations were also investigated by Krist & Hook (2003) from the crowded field of 47 Tuc. Such an analysis was not possible for individual GEMS fields because of the small number of stars ( $\sim 10$ ) per field. Thus, a simultaneous characterization of the spatial and temporal variations was not possible. However, since the spatial variations dominate (further details of our investigations of the ACS PSF variations will be given in a dedicated technical paper; K. Jahnke et al. 2004, in preparation), we used the large number of unsaturated stars in the GEMS area to construct an empirical PSF individually for each object. At a given position we combined the nearest  $\sim 35$  undisturbed stars to create a position-specific PSF estimate. In this way we averaged over time, but only stars from a radius  $\lesssim 40''$  were used, and PSF shape errors due to *spatial* variation were minimized, while a very high signal-to-noise ratio (S/N) was achieved for each of these PSF estimates. Finally, the subimage of each AGN and its connected PSF were registered to a common centroid.

From our PSF analysis we found that while coherent large-scale variations were essentially absent within each stack of  $\sim 35$  PSF stars, there was still considerable mismatch between the individual stars, in particular, in the central pixel regions. As such mismatched pixels could be spuriously assigned to a host galaxy, we took the variations within each PSF stack to derive rms frames describing an inherent PSF uncertainty; these were then also included in the variance images, artificially reducing the weight in the inner pixel regions. PSF rms errors per pixel range from up to 30% in individual pixels inside 1 FWHM, to 5%–15% inside  $0''.2$ , and to generally below 5% outside.

### 3.3. Peak-scaled PSF Subtraction

For luminous AGNs at high redshifts, separating the galaxy image from the nuclear point source is a daunting task. Even with a very good knowledge of the PSF, the problem is still that the relative scalings of galaxy and AGN are not known a priori. In fact, one cannot even be certain that the host galaxy is detectable at all and not swamped by the central point source. We therefore started out with the well-established technique of simple PSF subtraction.

In each case, the PSF was scaled to the central flux of the AGN and integrated inside a circular aperture of 4 pixel ( $0''.12$ ) diameter centered on the nucleus. This radius encircles approximately 34% of the total energy of a point source. A smaller radius (e.g., 1 pixel) would become too sensitive to shot noise and PSF mismatch, while larger radii would contain a significantly higher fraction of the total flux (50%, 60%, and 70% at 3, 4, and 5 pixel radii, respectively) and thus would make a detection of any host galaxy component successively more difficult.

This procedure somewhat oversubtracts the nuclear component by an amount corresponding to the underlying host galaxy contribution inside the encircled region. However, this method yields strictly conservative estimates of the host galaxy flux, i.e., always underestimating it. We used extensive simulations to determine correction factors for this oversubtraction (see § 3.6). The peak-scaled PSF subtraction method has the advantage of being independent of any assumption about the host galaxy morphology.

### 3.4. Two-dimensional Deblending

As a second method we employed the modeling package GALFIT, version 1.7a (Peng et al. 2002), which allows the simultaneous fitting of several two-dimensional components to an image, convolved with a given PSF. We describe our application of GALFIT to quasar images in Sánchez et al. (2004) in detail.

In total we ran GALFIT in three configurations, always fitting two components, which were the point-source nucleus and either an exponential disk (Freeman 1970), an  $r^{1/4}$  de Vaucouleurs spheroid (de Vaucouleurs 1948), or a Sérsic (1968) model with the Sérsic index as a free parameter. However, simulations (§ 3.6) showed that with the present data, the GALFIT version used<sup>9</sup> was operating near its limit because of the very high contrast between nuclei and host galaxies. In the context of this paper, we thus used GALFIT only as a cross-check on the peak subtraction method.

### 3.5. Detection Sensitivity

To determine the limits for detecting host galaxies we constructed a sample of 200 randomly selected unsaturated stars, 100 in each observed band, to mimic unresolved quasars. This way we could investigate how our nucleus-removal techniques responded to an undetectable host galaxy, and we could set limits on the size and shape of expected residuals and thus set lower flux limits for detectable host galaxies. For these stars the PSFs were created in exactly the same way as for the AGNs. The object itself was always excluded in the PSF production; thus, each test star and its PSF were fully independent.

<sup>9</sup> The GALFIT, version 1.7a, was recentering the PSF to given coordinates using a convolution with a narrow Gaussian, not by shifting the PSF by means of rebinning to a new position. The latter is better for the application to AGN decomposition and is now incorporated in later versions of GALFIT.

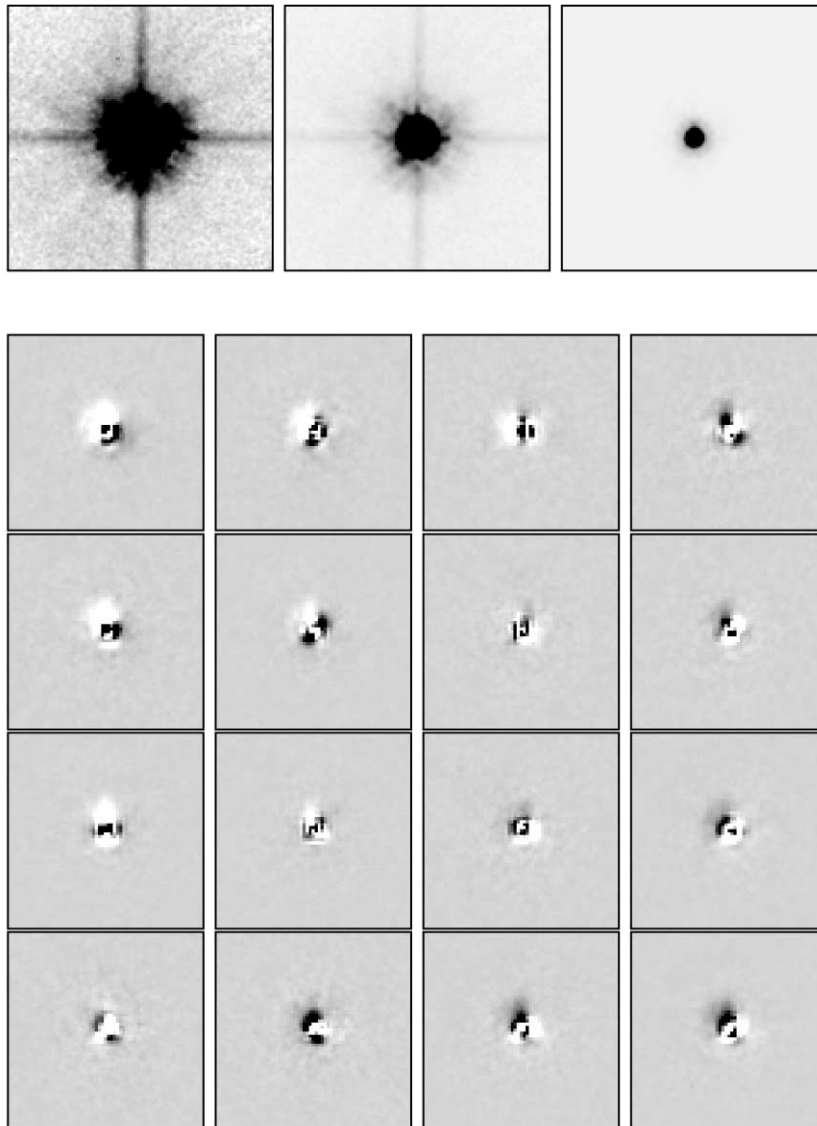


FIG. 2.—*Top*: PSF in the F606W band, shown with three display levels to enhance structures (size is  $3''.84 \times 3''.84$ ). *Bottom*: Subtraction of a total mean PSF from the PSFs in each of  $4 \times 4$  subtile regions to show the spatial variations of the PSF in the inner region (size is  $1''.92 \times 1''.92$ ). [See the electronic edition of the *Journal* for a color version of this figure.]

This set of simulated “naked quasars” showed that in 88% and 97% of all cases, any residuals—which could be taken as spurious (g)host galaxy detections—had fluxes of less than 5% and 10%, respectively, of the total object flux. From this we adopted the condition that a real detection should show a residual flux after peak subtraction of at least 5% of the total flux, corresponding to a maximum nucleus-to-host ratio of 20. Because of the systematic oversubtraction inherent in the procedure, corrections for the flux have to be applied (see § 3.6).

The final decision of whether a host galaxy was resolved was based on this criterion. In addition, we visually inspected whether the detected flux indeed came from a host galaxy or whether other, unmasked structures were present, using the peak-subtracted images and radial profile. If this could be ruled out we classified a host galaxy as detected.

### 3.6. Systematic Offsets and Errors

While the mere detection of an AGN host galaxy can be achieved with comparably little effort, the determination of flux error bars and systematic offsets is much more complicated. We performed extensive simulations of artificial quasar

images, composed from empirical PSFs and host galaxy models plus artificial noise matching the actual flux and noise distribution in real images. These simulations are described in detail by Sánchez et al. (2004). We applied the peak-subtraction nucleus removal, as well as GALFIT, to a set of  $\sim 2000$  quasar images created in this way. Comparing input and output parameter values yielded mean magnitude offsets, as well as statistical errors, for the individual host galaxy magnitudes (Fig. 3).

The simulations give reliability regions and error bars. Figure 3 (*left*) shows which magnitudes are recovered for a given synthetic host galaxy. Since the input set covers a large range of different morphological configurations, scale lengths, nucleus-to-host ratios, etc., the recovered values will scatter. Close to the detection limit, the scatter and the corrections grow rapidly as a function of magnitude; in addition, the ability to differentiate between morphological types will generally be lost. The combination of these effects is reflected in the spread of the output of the simulations. This measured spread is a direct estimate for the uncertainties of the total flux (Fig. 3, *right*).

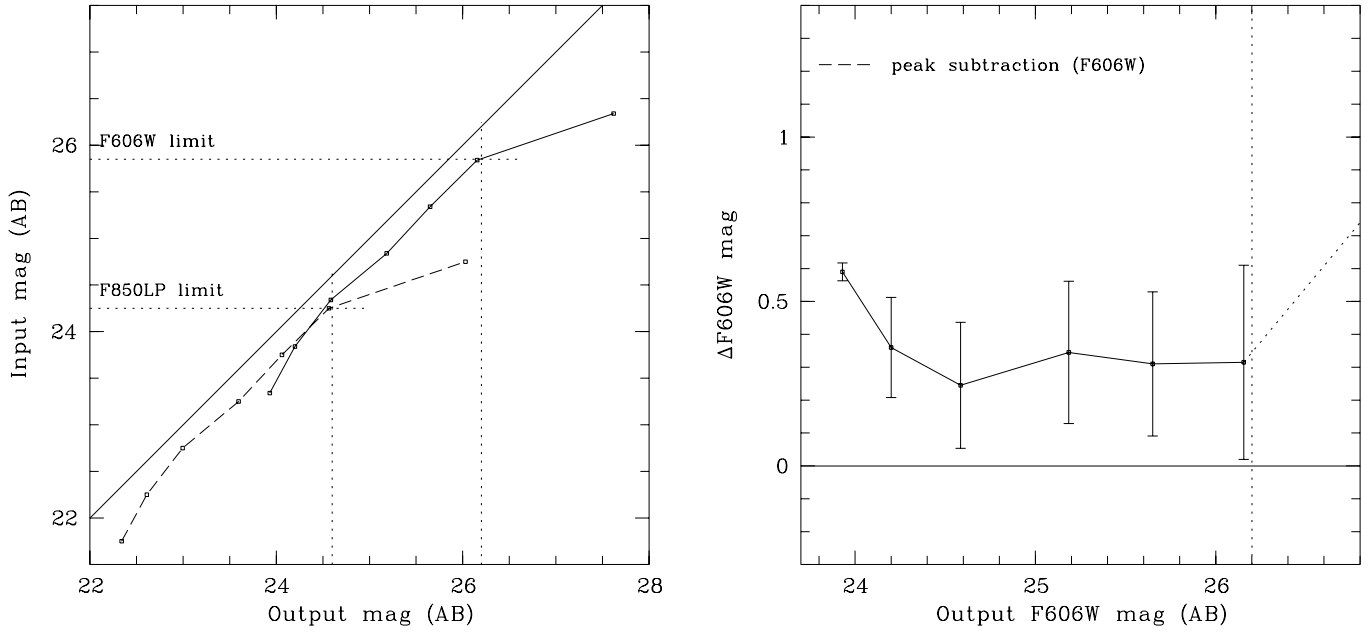


FIG. 3.—Simulation results on systematic offsets and errors in recovered host galaxy magnitudes. *Left*: Recovered host magnitude as a function of input magnitude for a range of morphologies, differing in scales and nucleus-to-host flux ratios matching our sample, for the two bands. The adopted reliability regions end at the dotted straight lines (see text). The F606W and F850LP bands are simply shifted with respect to each other by their zero-point offset ( $ZP_{F606W} - ZP_{F850LP} = 1.59$ ). *Right*: Difference of input and output magnitudes  $\Delta m$  vs. output F606W-band magnitude of the mean relation to the left. The overplotted errors are the  $1\sigma$  error ranges of the measured spread of host galaxy flux, as determined from the set of simulations with different parameter combinations and different noise realizations (see text). The vertical line gives the edge of the reliability region for the F606W band as above. For the F850LP band, again the zero point has to be shifted.

From these simulations we adopt approximate regions in brightness where host galaxy magnitudes can be reliably determined, with corrections of 0.25 to a maximum of 0.6 mag. These regions go down to F606W = 26.2, F850LP = 24.6 for the peak-subtraction method and the present data. On the outside, the corrections and errors increase. In three cases, marked in Table 2 with question marks in the  $Z_{\text{hg}}$  column, the observed magnitudes extend to outside these regions; here we continue using the derived corrections for these three objects, but the host galaxies thus derived are more uncertain, and their

magnitudes should be taken with care. Note that the F850LP-band data are substantially shallower than those in the F606W band, mainly a consequence of the ACS detector sensitivity.

## 4. RESULTS

### 4.1. Detected Host Galaxies

Using the above criteria for detecting a residual host galaxy, we find nine of the 23 host galaxies to be resolved in both bands, although some lie close to the sensitivity limit. One

TABLE 2  
PHOTOMETRY RESULTS FOR THE F606W ( $V$ ) AND F850LP ( $Z$ ) BANDS

ID	Tile	$V_{\text{tot}}^a$	$V_{\text{hg}}^b$	$V_{\text{hg,cor}}^c$	$V_{\text{nuc,cor}}^d$	$N/H_{V,\text{cor}}^e$	$Z_{\text{tot}}^a$	$Z_{\text{hg}}^{b,f}$	$Z_{\text{hg,cor}}^c$	$Z_{\text{nuc,cor}}^d$	$N/H_{Z,\text{cor}}^e$
19965.....	23	20.59	23.9	$23.3 \pm 0.05$	20.7	11.3	20.29	23.8	$23.5 \pm 0.2$	20.4	17.5
30792.....	82	21.60	24.6	$24.4 \pm 0.2$	21.7	12.0	22.06	24.2	$23.9 \pm 0.2$	22.3	4.2
18324.....	19	22.00	23.6	$23.0 \pm 0.05$	22.5	1.6	21.33	22.7	$22.4 \pm 0.2$	21.9	1.6
05498.....	01	22.91	25.5	$25.2 \pm 0.2$	23.1	7.1	22.28	25.0?	$24.4 \pm 1.2$	22.5	6.0
51835.....	55	23.01	26.0	$25.7 \pm 0.3$	23.1	11.2	22.41	23.8	$23.4 \pm 0.2$	23.0	1.6
00784.....	05	23.28	25.0	$24.7 \pm 0.2$	23.6	2.8	22.80	24.0	$23.7 \pm 0.2$	23.4	1.2
05696.....	02	22.73	24.7	$24.4 \pm 0.2$	23.0	3.6	22.32	23.8	$23.5 \pm 0.2$	22.8	1.9
05696.....	03	23.14	24.2	$23.9 \pm 0.15$	23.9	0.9	22.68	24.0	$23.7 \pm 0.2$	23.2	1.6
07671.....	07	22.35	25.6	$25.2 \pm 0.2$	22.4	13.2	22.24	25.0?	$24.4 \pm 1.2$	22.4	6.3
07671.....	15	22.36	25.5	$25.1 \pm 0.2$	22.5	11.9	22.22	24.6	$24.3 \pm 0.3$	22.4	5.5
11922.....	11	22.65	24.9	$24.6 \pm 0.2$	22.9	4.8	21.93	25.2?	$24.5 \pm 1.5$	22.0	9.3
Stack.....		21.47	24.9	$24.3 \pm 0.05$	21.6	12.3	21.60	U	U		

NOTES.—All magnitudes are uncorrected for Galactic extinction,  $A(\text{F606W}) = 0.024$  and  $A(\text{F850LP}) = 0.014$ . “U” marks an unresolved host galaxy.

<sup>a</sup> Total magnitude of the object.

<sup>b</sup> Raw measured host galaxy magnitude.

<sup>c</sup> Host galaxy magnitude corrected for oversubtraction.

<sup>d</sup> Corrected nuclear magnitude.

<sup>e</sup> Nuclear-to-host galaxy flux ratio.

<sup>f</sup> Values ending with a question mark lie outside the adopted reliability region (see text).

object formally fell above the 5% level in one band but not the other; COMBO-17 33630 at  $z = 2.719$  might be marginally resolved in F850LP and shows a structure at  $1''$  distance that might be a tidal arm or a foreground object. With this object lying at the highest redshift of the sample, we do not consider this a clear detection. As mentioned, for three further cases in the F850LP band, the host galaxies are very faint (marked with a question mark in the  $Z_{\text{hg}}$  col. in Table 2). While their flux is above 5% of the total, their raw magnitudes fall 0.8–1.0 mag outside the reliability region, where corrections and associated errors are still small. This low S/N is also reflected in the radial profiles (see the Appendix).

As described above, tests with field stars show that 12% of all objects (approximately three objects) might show spurious “host galaxies” at the 5% flux level, and 3% (zero or one objects) at the 10% flux level. In F606W five of our objects fall with their host fluxes between these two values. In the F850LP band there are four that include the three uncertain ones from above. According to statistics, one to three of these might be spurious detections. However, including or excluding these more uncertain data points in the following analysis does not have an influence on the conclusions drawn.

For each object the host galaxy flux was determined by simple aperture photometry after subtraction of the scaled PSF, excluding resolved companion objects. The radius of the aperture was matched to the image size used.

All extracted magnitudes are collected in Table 2 and shown together with the upper limit for the unresolved objects in the top panels of Figure 4. The extracted host galaxy images and radial surface brightness profiles are shown in Figure 11 in the Appendix. To illustrate the behavior of true point sources, we included a selection of 24 field stars, 12 each in the F606W and F850LP bands (Figs. 12 and 13), that were subjected to the same PSF determination and peak subtraction as described in § 3.5. We plot the same profiles as for the AGNs. This selection is random apart from the fact that the 24 stars were observed on 24 different tiles. For most of the stars there is no systematic positive residual flux visible, as expected. The few that do show positive fluxes form the spurious detection statistic described above.

While with deeper images or at lower redshift (Sánchez et al. 2004) the morphological appearance of the host galaxies can be determined, this was generally not possible for the present data. Apart from the extensions in COMBO-17 00784, apparent residual structure visible in the color images shown in the Appendix is dominated by the PSF subtraction procedure. This includes elongations and apparent off-centering due to limited centering precision of the order of 0.05–0.1 pixels (see, e.g., COMBO-17 05696 from tile 2). Thus, we adopted the host galaxy morphological class in all cases as “undecided” and then applied the systematic corrections for oversubtraction provided by the simulations (Fig. 3). The corrections were typically of the order of  $\sim 0.4$  mag, as documented by the columns with “cor” subscripts in Table 2. Here we also list the estimated uncertainties resulting from our extensive simulations. The distribution of corrected magnitudes is displayed in the bottom panels of Figure 4.

#### 4.2. Detecting the Undetected Hosts

For 14 AGNs we find that the individual PSF-subtracted residuals are consistent with nondetections, i.e., the magnitudes of individual host galaxies lie below the 5% limit. These objects are marked by arrow symbols in Figures 4 and 8. It is interesting to note that these flux limits on the hosts are by no

means all outstandingly faint. For many, the reason why they were not detected is the high contrast with the AGN, which for these objects has above average brightness. Only three objects show nondetections that indicate exceptionally faint host galaxies. We further discuss the implications of the detection limits in § 5.1.

In an attempt to assess at least the mean host galaxy properties of the unresolved AGNs, we simply co-added the images of all 14 objects, one of which was observed in two frames. This yielded a very deep image with effectively 15 orbits of integration time. We also combined their PSFs, weighted by the relative flux of the AGNs, and created combined variance and PSF rms frames. The higher S/N in combination with the lower PSF noise (PSF and AGN position are sampled at 14 different subpixel points) yields a nominal increase in surface brightness sensitivity of  $\sim 1.5$  mag. The resulting “object” has a mean redshift of  $z = 2.3$  (weighted by AGN flux) and total magnitudes of  $m_{\text{F606W,tot}} = 21.5$  and  $m_{\text{F850LP,tot}} = 21.6$ , respectively. This image is shown in Figure 5. With the higher sensitivity we now indeed find a host galaxy component in the F606W-band image after PSF subtraction of 4.4% of the total flux. The radial surface brightness profile also shows a small excess over an unresolved point source. In both cases this flux is highly significant, as we confirmed using a bootstrap simulation for the composition of the co-added frame from the 15 frames. In the bootstrap simulation we constructed 100 new sets of 15 frames each, drawn with repetition from the original 15 frames, co-added the images in each set, and did the flux analysis as above. The uncertainty in the total flux estimated from these 100 realizations is  $\sigma = 1.05\%$  of the total flux, or 25% in host galaxy flux. All realizations yielded substantial positive fluxes. The error results from a combination of PSF uncertainty and the noise inside the scaling aperture of 4 pixel diameter. We show the uncertainties in the radial surface brightness determined from bootstrapping as error bars for the derived host galaxy in Figure 5. The magnitudes thus extracted for host galaxies and nuclei in the F606W band are listed in the last row of Table 2 (the “stack” object). The F850LP-band stack, however, with its lower sensitivity, showed a much weaker signal than the F606W band, too faint to reliably be classified as resolved.

## 5. DISCUSSION

### 5.1. UV Colors

From the corrected magnitudes we have derived (F606W–F850LP) colors for the detected host galaxies. These are listed in Table 3, also including correction for Galactic dust extinction. However, with  $E(B - V) = 0.008$  (Schlegel et al. 1998) these values of  $A(\text{F606W}) = 0.024$  and  $A(\text{F850LP}) = 0.014$  negligibly affect the colors.

At these redshifts, the observed photometric bands correspond to the rest-frame UV, ranging from 2160 Å at  $z = 1.8$  to 1616 Å at  $z = 2.75$  in F606W and 3150–2350 Å in F850LP, respectively, so for this redshift range pure rest-frame UV colors are observed. Figure 6 shows the measured values plotted against  $z$ . There is no discernible color trend with redshift. All points fall within a relatively narrow range of colors; apart from COMBO-17 51835, the objects occupy a band of  $-0.2 < (\text{F606W} - \text{F850LP})_{\text{observed}} < 1.0$ . The open symbol represents our stacked average AGN constructed from the 14 unresolved objects. Although it was not resolved in the F850LP band, the upper limit on its color is actually

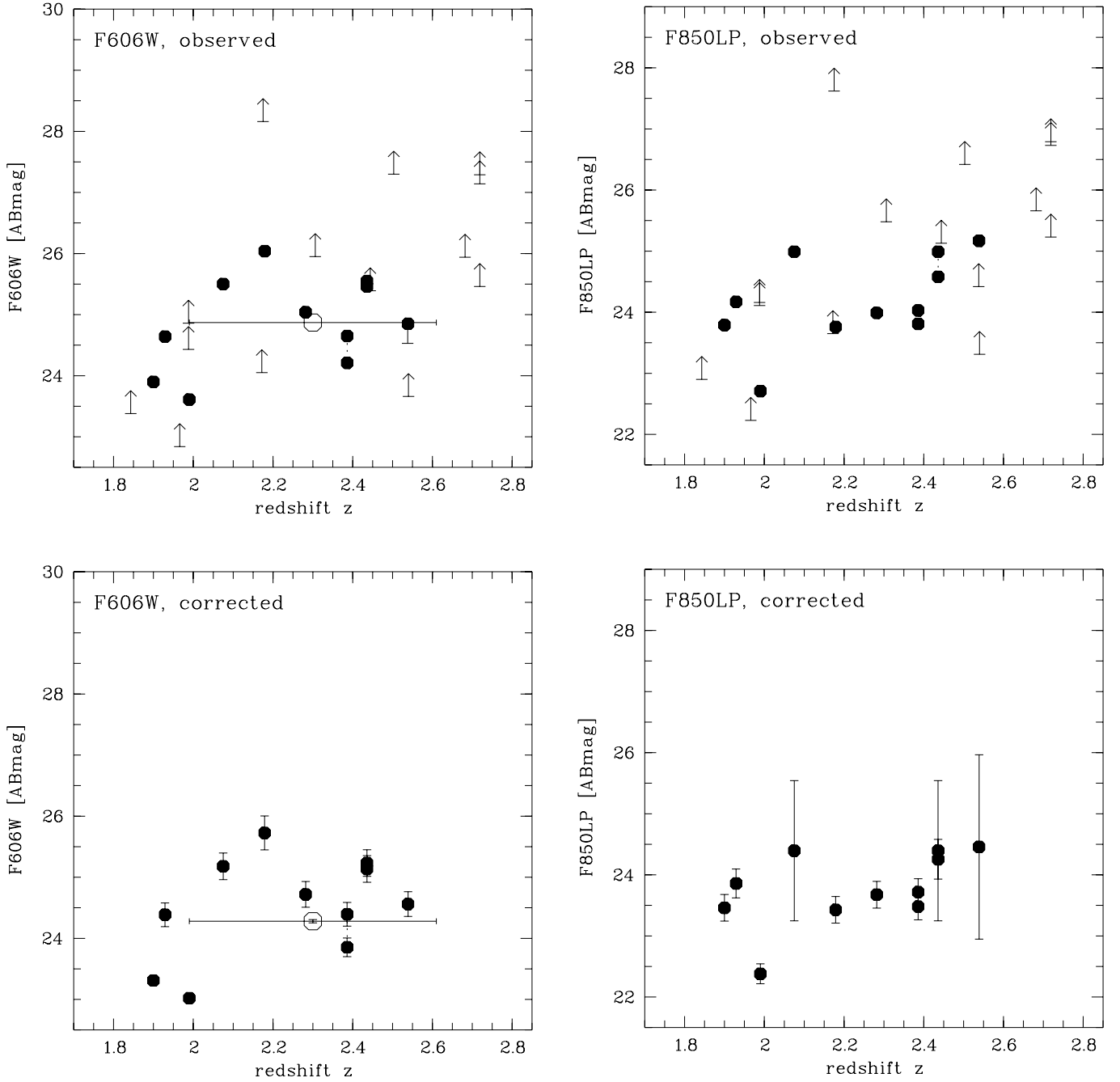


FIG. 4.—Peak-subtracted host galaxy magnitudes. *Top panels*, uncorrected for oversubtraction; *bottom panels*, corrected; *left panels*, F606W; *right panels*, F850LP. The arrows give upper limits for the unresolved host galaxies, and the open symbol for F606W is the host galaxy extracted from the stacked unresolved AGN images. The horizontal error bar for the stack gives the  $1\sigma$  redshift range of the co-added AGNs. In the bottom diagrams the vertical errors are uncertainties from the subtraction of the nucleus and are given as determined from the simulations (see § 3.6, Fig. 3).

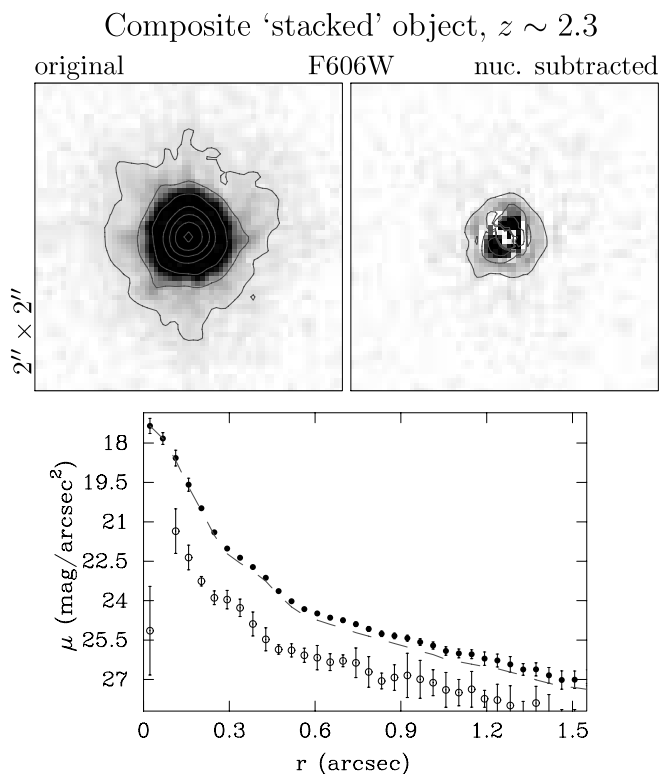


FIG. 5.—Stacked image of individually unresolved host galaxies. *Top*: Gray-scale original image and PSF-subtracted host galaxy image (both show  $2'' \times 2''$ ) in the F606W band. On top of the linear gray-scale plot, logarithmic contours with 0.5 dex spacing are overplotted. *Bottom*: Radial profiles of the F606W band. The curves show the upper data points with error bars from the original image, the PSF (dashed line), and the peak-subtracted host profile (lower points with error bars from bootstrapping). The host galaxy is shown without correction for any over-subtraction of the nucleus. [See the electronic edition of the Journal for a color version of this figure.]

consistent with the values derived for several of the detected objects.

One critical issue in measuring UV luminosities of barely resolved AGN hosts is the lingering possibility that flux may have spilled over from the nuclei. This could have happened as a purely observational artifact due to imperfect PSF re-

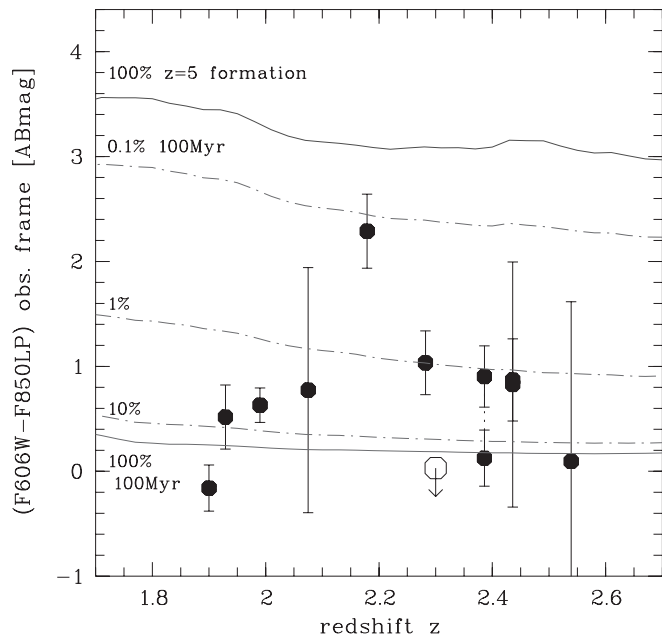


FIG. 6.—Observed colors (F606W – F850LP) of the sample from PSF peak subtraction (circles). The open symbol marks the upper limit for the stacked AGNs. Overplotted are two single-burst models (solar metallicity) from Bruzual & Charlot (2003) (solid lines). The upper curve is for a passively evolving burst at  $z = 5$ , and the lower for a burst of 100 Myr age, relative to each redshift. The dot-dashed lines are mixtures between the two, with a 0.1%, 1%, and 10% (top to bottom) fraction of mass of the 100 Myr population on top of 99.9%, 99%, and 90% of the  $z = 5$  population. [See the electronic edition of the Journal for a color version of this figure.]

moval, or physically by scattering of UV photons off dust in the host galaxy. The latter phenomenon is known to be relevant in high-redshift radio galaxies (Vernet et al. 2001). Independently of the underlying mechanism, any such cross-contamination should be visible in a correlation of host galaxy with nuclear colors. Figure 7 shows these colors plotted against each other. No correlation is visible, and we conclude that a substantial contamination of the host galaxy light from the AGN is very unlikely. Note also that when considering physical scattering in the hosts, powerful radio galaxies are

TABLE 3  
OBSERVED (F606W – F850LP) COLORS AND STAR FORMATION RATES FOR THE RESOLVED HOST GALAXIES AND THE STACKED AGNS IN THE CASE OF COLORS PRODUCED BY CONSTANT STAR FORMATION

ID	Tile	$z$	(F606W – F850LP) <sup>a</sup>	SFR F606W <sup>b</sup> ( $M_{\odot} \text{ yr}^{-1}$ )
19965.....	23	1.90	$-0.2 \pm 0.2$	11
30792.....	82	1.929	$0.5 \pm 0.3$	4
18324.....	19	1.990	$0.6 \pm 0.2$	15
05498.....	01	2.075	$0.8 \pm 1.2$	2
51835.....	55	2.179	$2.3 \pm 0.4$	1.5
00784.....	05	2.282	$1.0 \pm 0.3$	4
05696.....	02	2.386	$0.9 \pm 0.3$	6
05696.....	03	2.386	$0.1 \pm 0.3$	9
07671.....	07	2.436	$0.8 \pm 1.2$	3
07671.....	15	2.436	$0.9 \pm 0.4$	3
11922.....	11	2.539	$0.1 \pm 1.5$	5
Stack.....		2.3	$<0.0$	6

<sup>a</sup> Galactic extinction corrected.

<sup>b</sup> SFRs inferred from the UV flux in the observed F606W band.

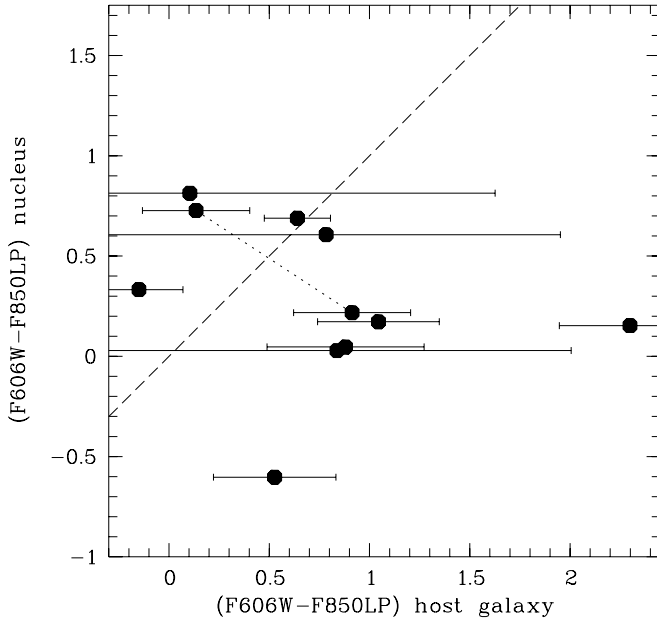


FIG. 7.—Nuclear vs. host galaxy colors for the objects in the sample with available colors. The two objects imaged twice are connected with a dotted line (in one case, not visible to near identical colors). The dashed line is the 1:1 relation to guide the eye.

huge massive entities of generally vastly different appearance compared to the relatively modest AGN hosts featured in our sample.

UV colors can be converted to UV spectral slope  $\beta$  independently of redshift, when assuming that the SED can be described in the form  $F_\lambda \propto \lambda^\beta$ . With  $\beta$  known, the absolute

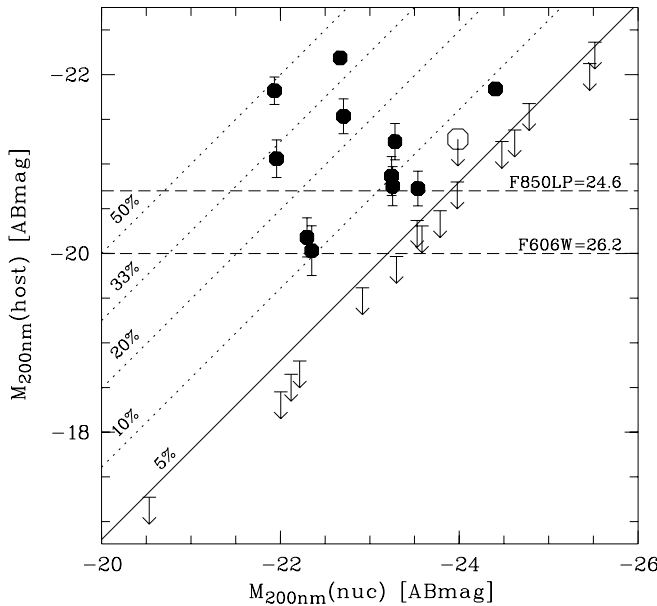


FIG. 8.—Nuclear vs. host galaxy absolute magnitude at 200 nm. Shown are objects with resolved host galaxies (*filled symbols*), the co-added stacked object (*open circle with upper limit arrow*), and upper limits for objects with unresolved hosts (*arrows*). The diagonal lines mark positions where the host galaxy light is a constant fraction of 5%, 10%, 20%, 33%, and 50% of the total light, assuming a constant spectral slope  $\beta$ . The horizontal dashed lines show the magnitudes of host galaxies at the F606W = 26.2 and F850LP = 24.6 mag detection limit, at mean redshift and mean  $\beta$ .

magnitude at 200 nm,  $M_{200\text{ nm}}$ , can be computed directly from the F606W- or F850LP-band apparent magnitudes. We do this for both the host and the nucleus, and these values are shown for the full sample, including upper limits, in Figure 8, which illustrates the two main constraints for resolving a host galaxy, apart from compactness (see § 4.2). The reliability of host galaxy photometry is constrained by the S/N and is thus dependent on the filters, which have different depths. This is marked by the horizontal dashed lines, which show the  $M_{200\text{ nm}}$  magnitude of host galaxies at the F606W = 26.2 and F850LP = 24.6 mag edges of the adopted regions of reliability (see § 3.6), at mean redshift and mean  $\beta$ .

As a second effect, the maximum nucleus-host contrast appears as the scatter of unresolved objects around a line shifted by 3.2 mag from unity, corresponding to 5% of the total flux. Here the scatter is only induced by the assumption that all unresolved host galaxies have a  $\beta$ -value at the upper limit determined for the stacked image. The diagonal dotted lines mark lines of 10%, 20%, 33%, and 50% of the total flux associated with the host galaxy. Thus, in total the region to the right of the solid diagonal line is inaccessible to host galaxy detection with the current data and method of analysis. We would like to emphasize that the similarity of nuclear properties for resolved and unresolved host galaxies suggests also that the host galaxy properties are similar, thus supporting that the data point for the co-added stacked object is not far off the individually resolved objects in all plots.

In Figure 9 the spectral slope is plotted against  $M_{200\text{ nm}}$  for the host galaxies and compared with the mean value for a sample of 794 Lyman break galaxies (LBGs) at redshift  $z \sim 3$  (Shapley et al. 2003), with all values uncorrected for the influence of dust in the galaxies. The slight anticorrelation that seems to be visible between  $\beta$  and UV luminosity suggests that the more luminous host galaxies have steeper spectral slopes or bluer colors. This would mean that more luminous host galaxies have bluer colors and thus more UV light from

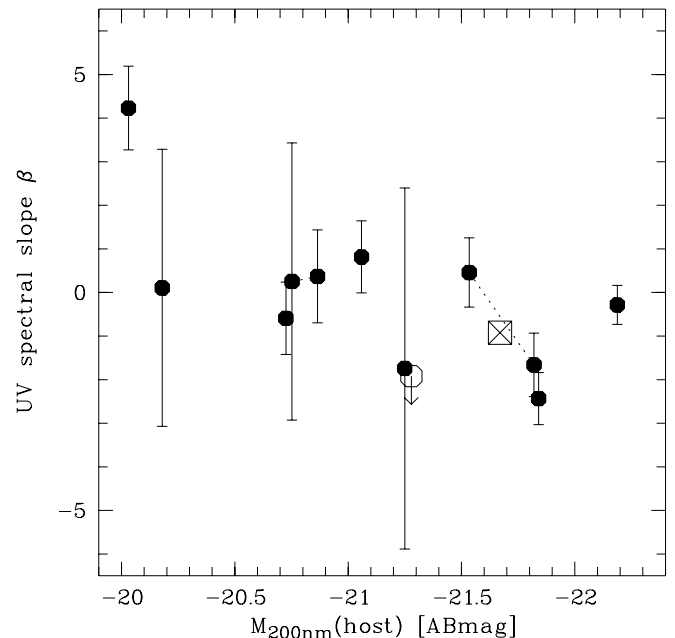


FIG. 9.—Spectral slope  $\beta$  in the UV ( $F_\lambda \propto \lambda^\beta$ ) vs. 200 nm absolute magnitude, uncorrected for dust. The open symbol marks the stacked object, and the crossed square shows the mean value obtained by Shapley et al. (2003) for 794 LBGs at  $z \sim 3$ .

young stars. To test this we computed the Spearman rank-order coefficient for this data set. The test gave a probability for the zero hypothesis (uncorrelated data) of 9%. Thus, the zero hypothesis cannot even be rejected on a  $2\sigma$  level, and the anticorrelation is not significant.

A few of the most UV-luminous host galaxies fall into the same magnitude-color regime as the LBGs, while a number of objects are substantially redder. Thus, we do not find a positive correlation between the amount of host UV light and luminosity.

### 5.2. Origin of the Host Galaxy UV Flux

The top solid line in Figure 6 shows the theoretical color of a galaxy that formed all its stars at  $z = 5$  and evolved passively afterward. This color was computed from single stellar population models taken from Bruzual & Charlot (2003). The assignment of solar metallicity in this context is arbitrary and subject to discussion (see below). However, qualitatively there is no strong dependence on metallicity, the exact formation redshift, or the particular choice of initial mass function (IMF) for a given model family (Salpeter 1955; Chabrier 2003) in this wavelength range.

This comparison shows that the measured UV colors of our detected AGN hosts, as well as of the stacked mean host galaxy, are markedly bluer than expected for an old population at that epoch, i.e.,  $t_{\text{age}} \sim t_{\text{Hubble}}$ . Any correction for dust in the host galaxies will strengthen this result. Thus, the blue light detected in these galaxies must come from relatively young stars. These stars could be forming continuously, in which case the UV luminosities can be interpreted as indicators of the star formation rate (SFR) in these galaxies. We follow up on this option in § 5.2.2. Alternatively, the UV flux could be the afterglow of a past starburst. This is the option we consider first.

#### 5.2.1. Recent Starburst

Given the unknown dust absorption and metallicities in the host galaxies, a single UV color is insufficient for performing a detailed age dating of starbursts or a decomposition of stellar populations. However, we want to compare with the available theoretical color range spanned by galaxy formation at  $z = 5$  and a very recent (100 Myr) starburst to illustrate how mixing of an old underlying population with most of the mass and a recent starburst influences the color. In Figure 6 the solid lines mark these extremes. In between these the dot-dashed lines show how the contribution of a 100 Myr component would influence the color of an otherwise old population. From top to bottom, 0.1%, 1%, and 10% in mass are added to the old population. There is a strong degeneracy between the choice of burst age and the mixing ratio. For 10 Myr, less than one tenth the mass is required to produce the same UV color compared to that required for 100 Myr. If we choose 100 Myr as a timescale similar to the dynamical timescale in galaxies, the masses involved in that starburst would be of the order of a few percent of the total stellar mass.

For the assumption of only one single-aged population, we can rule out very high formation redshift;  $z = 5$  corresponds to ages of 3.5–2.5 Gyr at  $z = 1.8$ –2.5 in the chosen cosmology. For the adopted set of models, the resulting age estimates would range mostly between  $\sim 0.1$  and  $\sim 0.7$  Gyr.

We note that the color tracks in Figure 6 are largely flat over the redshift range of interest and that the two pure populations

and the different mixing ratios correspond to different colors almost independently of  $z$ . Since our measured colors are all quite similar, we conclude that the luminosity-weighted ages of the UV-dominating stellar population must be rather similar, unless younger ages and more reddening in some objects conspire.

Clearly, a single UV color is insufficient to perform a reliable age dating, with all broadband colors being affected by various degeneracies with respect to dust and metallicities. However, we have reason to believe that at least the central lines of sight toward the AGNs are reasonably free of dust extinction (because the AGN sample is selected by optical/UV flux), and we therefore do not expect dust to play a major role. At any rate, significant dust extinction would make the host galaxies intrinsically bluer than what we observe. On the other hand, assuming a metallicity lower than solar would shift all curves in Figure 6 downward, resulting in older age estimates. Reducing the metallicity to  $Z = 0.004$  (one-fifth solar) gives a single burst age increase by a factor of 2 (for Bruzual & Charlot [2003] models). We conclude that if the UV light in our host galaxies is emitted by a passively evolving population of young stars, this population is typically much younger than 1 Gyr.

The diagram in Figure 8 shows that no correlation exists between the amount of stellar UV light from the host galaxies and the amounts of UV radiation produced by the nuclei. If the latter is taken as a measure of the amount of matter accreted by the nuclei, then in the context of a recent starburst the size of the starburst and the amount of accreted matter must be governed by different mechanisms. If the accretion rate is primarily defined by the nuclear mass and a correlation between galaxy and black hole mass is assumed, then the size of the starburst is independent of the bulk stellar mass of the host galaxy. Other factors must be dominating the amount of (gas) mass involved in the starburst. This can be the total amount of gas available in the galaxy, the size of the region involved in the starburst, the strength of the interaction responsible for the starburst, etc. In any case, the amounts of gas involved are variable for a given nuclear luminosity. Including the upper limits in Figure 8, the host luminosities span, e.g.,  $\sim 4$  mag at  $M_{200\text{ nm}}(\text{nuc}) = -22$ , i.e., the amount of gas involved can vary by a factor of  $\sim 40$  or more.

#### 5.2.2. Estimating a Host Star Formation Rate

We now interpret the detected UV emission in the alternative framework as being due to young stars forming continuously in the AGN host galaxies. Under this assumption it is possible to estimate the SFR of the host galaxies from the measured rest-frame UV luminosities. Following Kennicutt (1998) and using the conversion of AB magnitudes into monochromatic fluxes, we obtain

$$\text{SFR}(M_{\odot} \text{ yr}^{-1}) = 1.8 \times 10^{-27} \left( \frac{d_l^2 10^{-0.4(m_{\text{AB}} + 48.6)}}{1 + z} \right),$$

where  $d_l$  is the luminosity distance to the AGN in centimeters and  $m_{\text{AB}}$  is the observed UV magnitude at an arbitrary wavelength between 1500 and 2800 Å. With this formula we can now convert our F606W-band luminosities (which are much deeper than the F850LP-band data) into SFRs. As long as intrinsic dust attenuation is neglected, these values are of course mere lower limits.

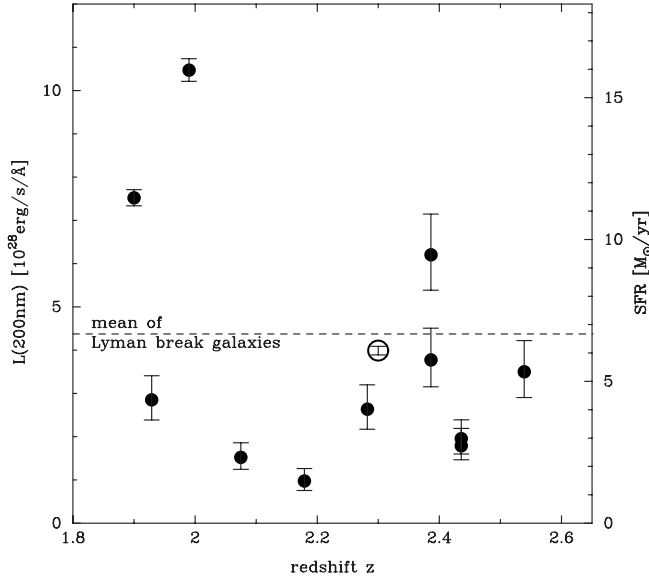


FIG. 10.—Rest-frame 200 nm luminosities and SFRs as derived from the F606W band, both uncorrected for dust. The open symbol marks the SFR of the stacked object created from the AGNs with individually unresolved host galaxies. The horizontal dashed line shows the value obtained by Erb et al. (2003) for LBGs at  $z = 2.5$ .

The resulting SFR values are listed in Table 3 and generally amount to a few solar masses per year, with remarkably little variation. The maximum value found is  $\sim 15 M_{\odot} \text{ yr}^{-1}$ , and the mean is  $\sim 6 M_{\odot} \text{ yr}^{-1}$ , including the results from the stacked image of individually unresolved host galaxies. This value is thus representative for the full sample of 23 AGNs. We show the distribution of SFRs versus redshifts in Figure 10. No trend emerges, consistent with the previously established observations that neither colors nor luminosities show any significant trend with  $z$ .

This is again compared with the SFRs for LBGs at  $z = 2-2.6$  from Erb et al. (2003), as determined from the UV flux and uncorrected for dust. There are a few host galaxies with higher UV fluxes, while for the majority it is smaller by a factor of 2–3.

However, there is a principal caveat in our guiding assumption in this subsection: The UV light from galaxies with strong ongoing star formation is expected to be totally dominated by the youngest stars. Kennicutt (1998) pointed out that the spectral shape of galaxies with a constant SFR over at least  $\sim 100$  Myr is basically flat (in  $f_{\nu}$ ) between 1500 and 2800 Å, assuming a Salpeter (1955) IMF. This would lead to an expected UV color for our objects of  $(m_{F606W} - m_{F850LP}) = 0$  or a spectral index  $\beta = -2$ , more or less independently of redshift (within the  $z$ -range of our sample), inconsistent with our observations for most objects (see § 5.1: Fig. 6 and Table 3). In other words, most detected host galaxies of our sample have UV colors that are too red for a simple continuous star formation scenario, while the stacked host galaxy is roughly consistent. If for the resolved hosts the F850LP-band fluxes were used instead of the F606W band, SFR values would be higher by roughly a factor of 2.

This apparent inconsistency could be resolved in several ways. The initial assumption could be wrong, and the UV flux could originate not from freshly formed stars but from a passively evolved starburst, as outlined in § 5.2.1. The SFR

might not have been constant over the past, so that varying amounts of stars of different masses and ages would have been formed; such a configuration is always possible, and our only argument against it would invoke Occam’s razor. Finally, as discussed in § 5.2.1, there could be an underlying older stellar population contributing more to F850LP and less to F606W (but note that by sample design, F850LP is completely below the Balmer jump at all relevant redshifts). This is the scenario that is favored by our intermediate-redshift data from GEMS (Sánchez et al. 2004).

Clearly, in this study our current data set of just two UV bands is insufficient to settle this ambiguity. However, in all three cases there would be no continuous star formation as inferred for LBGs. The blue light would be a result not of a continuous process but of one or more events in the past of the host galaxy that triggered star formation. Whether galaxy interaction or merger incidents were responsible or the formation of bars or spiral arms is involved cannot be investigated with the present set of data.

### 5.3. Comparison with Other AGN Host Galaxy Studies

Even at low redshifts, color data of AGN host galaxies are relatively scant, except for rather low-luminosity AGNs in which the host galaxy can be separated with relative ease. In those cases, colors were generally found to be consistent with morphological types, in particular for the prevailing disk-type host galaxies (Kotilainen & Ward 1994; Schade et al. 2000). However, when higher nuclear luminosities are observed (which generally correlate with a larger bulge component), then a tendency toward abnormally blue colors and younger stellar populations emerges (Kauffmann et al. 2003; Jahnke et al. 2004). This tendency appears to hold also at intermediate redshifts, as demonstrated in our companion *HST* paper (Sánchez et al. 2004), in which we find more than half of the investigated host galaxies to have bluer colors than what would be expected from their morphological types. However, we cannot confirm increasing amounts of blue light from young stars with increasing host luminosity as found by Kauffmann et al. (2003). Our data are consistent with constant UV flux for all hosts.

At high redshifts ( $z \gtrsim 2$ ), color information is available only for a handful of objects. In a ground-based study of six bright radio-loud quasars, Lehnert et al. (1992) found indications that the hosts were very blue, actively star-forming galaxies. For three high-luminosity quasars, one radio-loud and two radio-quiet, Aretxaga et al. (1998) claimed very luminous envelopes and SFRs of several hundreds of solar masses per year. More recently, Hutchings et al. (2002) presented optical *HST* observations of three radio-loud and two radio-quiet quasars and found less extreme but qualitatively similar results.

Because of their high radio power and optical luminosities, many of the quasars observed in previous studies are probably quite different from the moderate-luminosity hosts of moderate-luminosity radio-quiet AGNs that we focus on. It is nevertheless interesting to see that the presence of a significantly enhanced UV continuum and young stars seems to be at least qualitatively similar between QSOs of intermediate and high luminosities.

## 6. CONCLUSIONS

We performed the hitherto largest study of host galaxy properties of a complete sample of high-redshift AGNs. We

detected the hosts and extracted color information for nine of the 23 AGNs, and we also achieved a statistical detection of the host in the remaining 14 from a stack analysis. The UV luminosities can be interpreted in three ways: either as a contribution from a passively evolving population of relatively young stars, forming typically 0.5 Gyr ago, as a mix between a population of old (e.g.,  $t_{\text{age}} \sim t_{\text{Hubble}}$ ) stars and a small contribution from a recently formed young population (e.g., 0.1%–10% in mass at an age of 100 Myr or 1/10 of this for age 10 Myr), or as an indicator of ongoing star formation at a level of  $\sim 2\text{--}15 M_{\odot} \text{ yr}^{-1}$  (uncorrected for internal dust attenuation). While the first possibility is very simplistic and appears unphysical, the UV colors actually favor the two burst interpretations; but the possibility of ongoing star formation cannot be completely ruled out from our data.

In the framework of combined old and young populations, it is remarkable how similar the host galaxy colors are within the sample, and hence, unless different mass-age combinations conspire, the estimated stellar mass fractions and ages. The derived young population mass fractions and ages are also very similar to the values estimated in our companion GEMS study of AGNs at  $z \lesssim 1$  (Sánchez et al. 2004), where we find abnormally blue rest-frame  $U - V$  colors for a substantial fraction of host galaxies, particularly the most luminous AGNs in the sample. Even more, these colors and ages are in turn very close to the mean values obtained from our ground-based low- $z$  multicolor sample (Jahnke et al. 2004). While the stellar population diagnostics of Kauffmann et al. (2003) are not immediately convertible into our simple color indicators, their impressive and highly significant results point in exactly the same direction.

While the results from all these redshift regimes are similar and indicate a connection between nuclear activity and the presence of young stars and that mass fractions of young stars are similar, we always find that a larger range of absolute masses is involved, showing as a range in UV luminosity. Here we find a variation of a factor of  $\gtrsim 40$  for a given nuclear luminosity.

Our host galaxy colors span a range that reaches the colors of Lyman break galaxies for a few very luminous hosts, while, as mentioned, the colors of the majority are somewhat redder than these. A comparison of optical/UV properties

with the general population of high-redshift galaxies would be very illuminating, but large statistical samples will only become available in the near future, e.g., from the GOODS project.

This persistent trend of finding AGNs to be associated with blue stellar colors is intriguing and suggests a close connection between enhanced star formation and nuclear activity. Additional support for such a connection comes from the detection of submillimeter CO emission in a number of extremely luminous high-redshift QSOs and radio galaxies (Omont et al. 2003), although the current sensitivity of submillimeter telescopes is insufficient to perform this test for less luminous AGNs at high  $z$ .

While the fact that there is a relation can hardly be denied, its physical origin remains obscure. Is the enhancement of star formation a prerequisite for nuclear activity? Is it a simultaneously occurring phenomenon, caused by the same trigger? Or is it a consequence of the AGNs? Galaxy merging and interaction are clearly two possible candidates to connect these two phenomena, but they are not the only ones, nor are the involved physics understood. Much additional data will be required, in particular those helping reliably to reconstruct the star formation history in high-redshift galaxies, before any firm conclusions can be drawn.

This work is based on observations taken with the NASA/ESA *Hubble Space Telescope*, which is operated by the Association of Universities for Research in Astronomy, Inc. (AURA) under NASA contract NAS5-26555. Support for the GEMS project was provided by NASA through grant GO-9500 from the Space Telescope Science Institute, which is operated by AURA for NASA under contract NAS5-26555. E. F. B. and S. F. S. acknowledge financial support provided through the European Community's Human Potential Program under contract HPRN-CT-2002-00316, SISCO (E. F. B.), and HPRN-CT-2002-00305, Euro3D RTN (S. F. S.). C. W. was supported by the PPARC rolling grant in Observational Cosmology at the University of Oxford. S. J. acknowledges support from NASA under LTSA grant NAG5-13063 issued through the Office of Space Science. D. H. M. acknowledges support from NASA under LTSA grant NAG5-13102 issued through the Office of Space Science.

## APPENDIX

### AGN IMAGES AND SURFACE BRIGHTNESS PLOTS OF AGNs AND STARS

Figure 11 shows plots for each of the nine resolved objects plus the composite stacked object. Two objects appear twice, as they appear in overlapping GEMS tiles. Figures 12 and 13 show a random selection of isolated stars used to show the zero case of point sources without any host galaxy contribution, for comparison purposes.

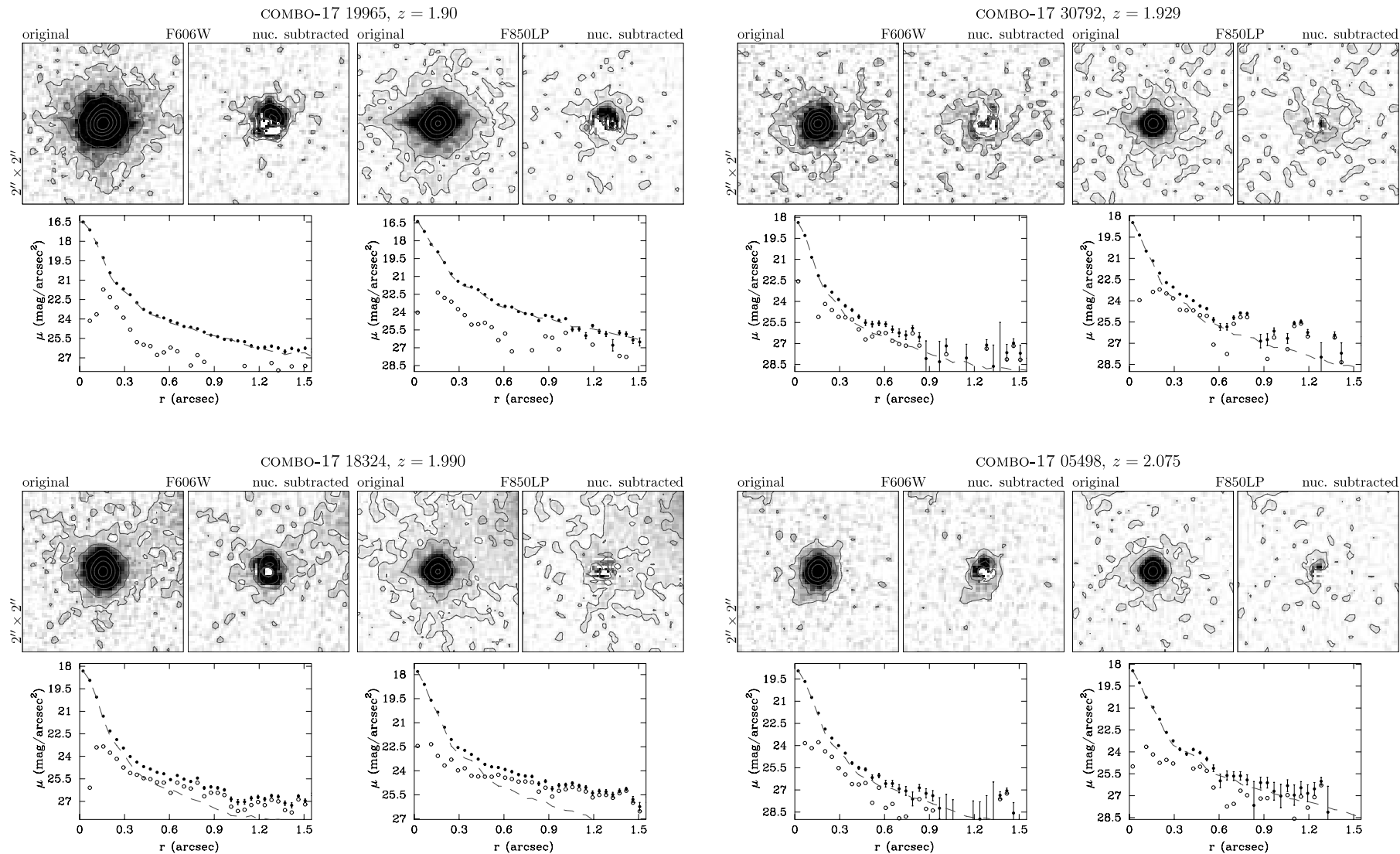


FIG. 11.—For each object, the original images and the uncorrected peak-scaled PSF-subtracted images for both the F606W and F850LP filters. The image size is  $2'' \times 2''$ , and the images are shown in a linear gray scale, with overplotted logarithmic isophotes of 0.5 dex spacing. The plots below for each object show the radial surface brightnesses in the two filters, respectively. The curves show the data points with error bars from the original image (*filled symbols*), the PSF (*dashed red line*), and the peak-subtracted host profile (*open symbols*). The host galaxy is shown without any correction for oversubtraction as applied to the derived magnitudes. [See the electronic edition of the Journal for a color version of this figure.]

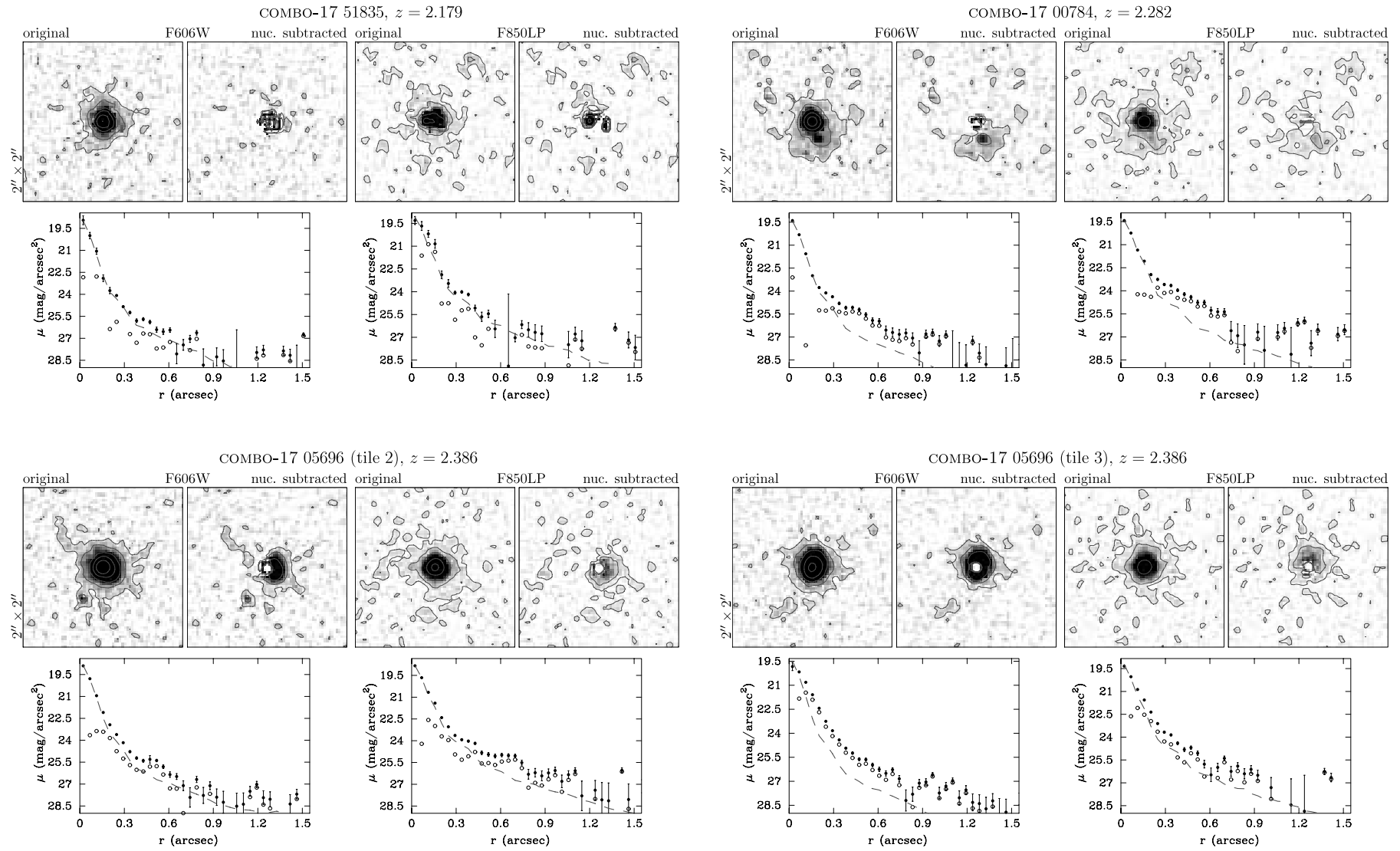


FIG. 11.—Continued

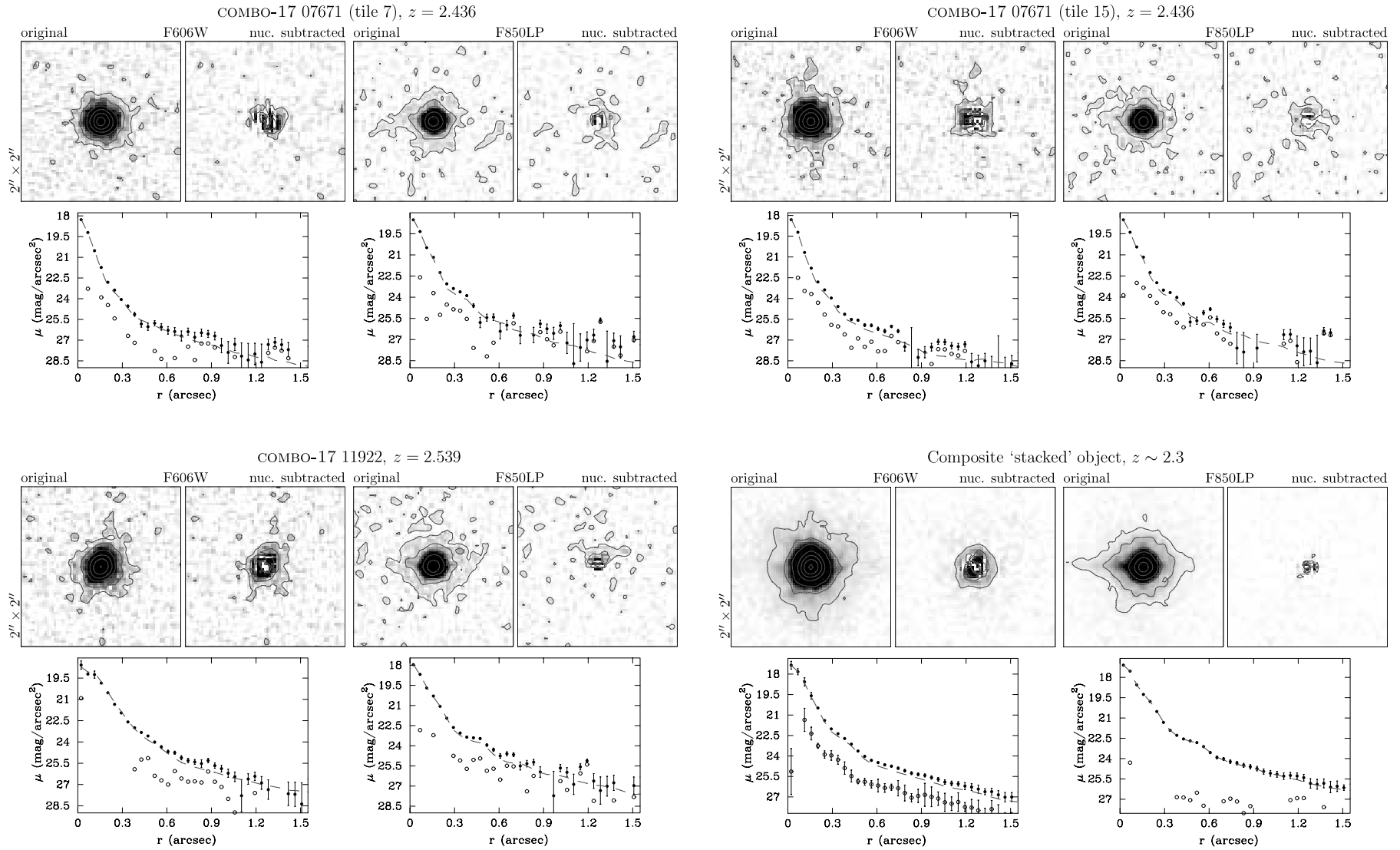


FIG. 11.—Continued

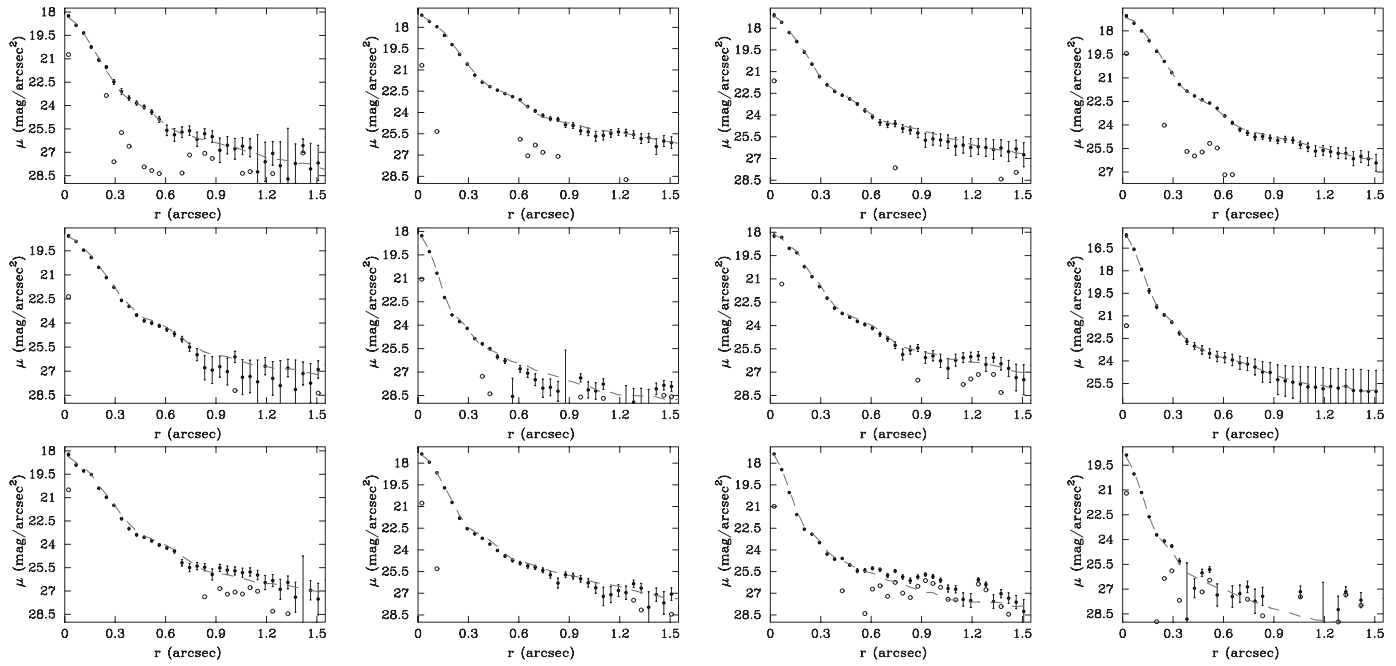


FIG. 12.—PSF peak subtraction applied to field stars for the F606W band. Shown are surface brightness profiles for 12 randomly selected field stars in the F606W band. Symbols and lines are as in Fig. 11. [See the electronic edition of the *Journal* for a color version of this figure.]

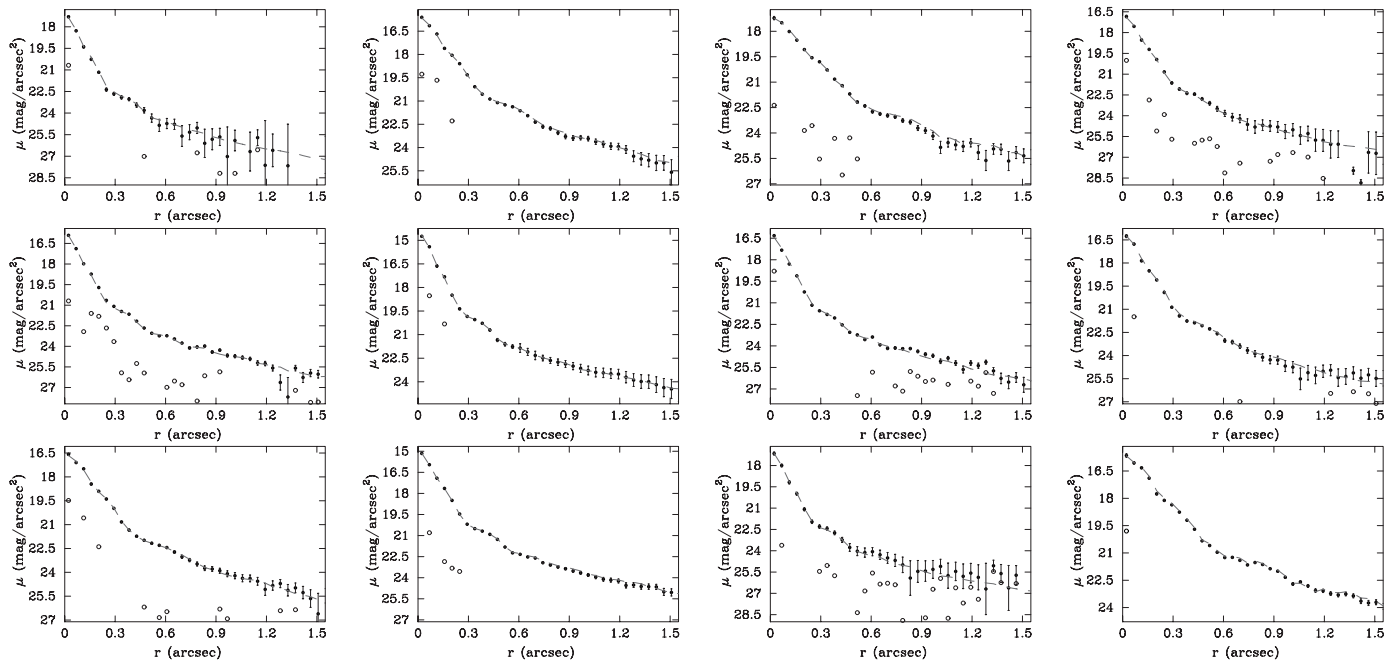


FIG. 13.—Same as Fig. 12 but for 12 different randomly selected stars in the F850LP band. [See the electronic edition of the *Journal* for a color version of this figure.]

## REFERENCES

- Aretxaga, I., Terlevich, R. J., & Boyle, B. J. 1998, *MNRAS*, 296, 643  
 Bruzual, G., & Charlot, S. 2003, *MNRAS*, 344, 1000  
 Carballo, R., Sánchez, S. F., González-Serrano, J. I., Benn, C. R., & Vigotti, M. 1998, *AJ*, 115, 1234  
 Chabrier, G. 2003, *PASP*, 115, 763  
 de Vaucouleurs, G. 1948, *Ann. d'Astrophys.*, 11, 247  
 Erb, D. K., Shapley, A. E., Steidel, C. C., Pettini, M., Adelberger, K. L., Hunt, M. P., Moorwood, A. F. M., & Cuby, J. 2003, *ApJ*, 591, 101  
 Falomo, R., Kotilainen, J. K., Pagani, C., Scarpa, R., & Treves, A. 2004, *ApJ*, 604, 495  
 Freeman, K. C. 1970, *ApJ*, 160, 811  
 Gebhardt, K., et al. 2000, *ApJ*, 539, L13

- Giavalisco, M., et al. 2004, *ApJ*, 600, L93
- Grogin, N. A., et al. 2003, *ApJ*, 595, 685
- Hutchings, J. B. 2003, *AJ*, 125, 1053
- Hutchings, J. B., Crampton, D., Morris, S. L., Durand, D., & Steinbring, E. 1999, *AJ*, 117, 1109
- Hutchings, J. B., Frenette, D., Hanisch, R., Mo, J., Dumont, P. J., Redding, D. C., & Neff, S. G. 2002, *AJ*, 123, 2936
- Jahnke, K., Kuhlbrodt, B., & Wisotzki, L. 2004, *MNRAS*, 352, 399
- Kauffmann, G., et al. 2003, *MNRAS*, 346, 1055
- Kennicutt, R. C., Jr. 1998, *ARA&A*, 36, 189
- Koekemoer, A. M., et al. 2002, *ApJ*, 567, 657
- Kotilainen, J. K., & Ward, M. J. 1994, *MNRAS*, 266, 953
- Krist, J., & Hook, R. 2003, ACS WFC and HRC Field-dependent PSF Variations Due to Optical and Charge Diffusion Effects (STScI Instrum. Sci. Rep. ACS 2003-06; Baltimore: STScI)
- Kukula, M. J., Dunlop, J. S., McLure, R. J., Miller, L., Percival, W., Baum, S. A., & O'Dea, C. P. 2001, *MNRAS*, 326, 1533
- Lehnert, M. D., Heckman, T. M., Chambers, K. C., & Miley, G. K. 1992, *ApJ*, 393, 68
- Omont, A., Beelen, A., Bertoldi, F., Cox, P., Carilli, C. L., Priddey, R. S., McMahon, R. G., & Isaak, K. G. 2003, *A&A*, 398, 857
- Peng, C. Y., Ho, L. C., Impey, C. D., & Rix, H.-W. 2002, *AJ*, 124, 266
- Ridgway, S. E., Heckman, T. M., Calzetti, D., & Lehnert, M. 2001, *ApJ*, 550, 122
- Rix, H.-W., et al. 2004, *ApJS*, 152, 163
- Salpeter, E. E. 1955, *ApJ*, 121, 161
- Sánchez, S. F., & González-Serrano, J. I. 2003, *A&A*, 406, 435
- Sánchez, S. F., et al. 2004, *ApJ*, 614, 586
- Schade, D., Boyle, B. J., & Letawsky, M. 2000, *MNRAS*, 315, 498
- Schlegel, D. J., Finkbeiner, D. P., & Davis, M. 1998, *ApJ*, 500, 525
- Schreier, E. J., et al. 2001, *ApJ*, 560, 127
- Sérsic, J. 1968, Atlas de Galaxias Australes (Córdoba: Obs. Astron. Univ. Nacional Córdoba)
- Shapley, A. E., Steidel, C. C., Pettini, M., & Adelberger, K. L. 2003, *ApJ*, 588, 65
- Vernet, J., Fosbury, R. A. E., Villar-Martín, M., Cohen, M. H., Cimatti, A., di Serego Alighieri, S., & Goodrich, R. W. 2001, *A&A*, 366, 7
- Wolf, C., Meisenheimer, K., Rix, H.-W., Borch, A., Dye, S., & Kleinheinrich, M. 2003a, *A&A*, 401, 73
- Wolf, C., Wisotzki, L., Borch, A., Dye, S., Kleinheinrich, M., & Meisenheimer, K. 2003b, *A&A*, 408, 499
- Wolf, C., et al. 2004, *A&A*, 421, 913